Enhanced photostability of cuprous oxide by lignin films on glassy carbon electrodes in the transformation of carbon dioxide

Journal:	*Green Chemistry*
Manuscript ID	GC-ART-02-2018-000365.R1
Article Type:	Paper
Date Submitted by the Author:	04-Apr-2018

Complete List of Authors:	Landaeta, Esteban; Pontificia Universidad Catolica de Chile, Quimica Inorganica Isaacs Casanova, Mauricio; Pontificia Universidad Catolica de Chile, Quimica Inorganica; Pontificia Universidad Catolica de Chile, Centro de Investigación en Nanotecnología y Materiales Avanzados.; Pontificia Universidad Catolica de Chile, UC-Energy Research Center. Schrebler, Ricardo; Pontificia Universidad Catolica de Valparaiso, Instituto de Química Schultz, Zachary; University of Notre Dame, Chemistry and Biochemistry; The Ohio State University, Department of Chemistry and Biochemistry Burgos, Ana; Pontificia Universidad Catolica de Valparaiso Facultad de Ciencias, Instituto de Química

Green Chemistry

PAPER

Enhanced photostability of cuprous oxide by lignin films on glassy carbon electrodes in the transformation of carbon dioxide

Received 00th January 20xx,
Accepted 00th January 20xx

DOI: 10.1039/x0xx00000x

www.rsc.org/

E. Landaeta[a], Zachary D Schultz[b,c], Ana Burgos[d], Ricardo Schrebler[d] and M. Isaacs[a,e,f]*

Photoelectrochemical reduction of CO_2 was investigated on carbon electrodes modified with lignin and cuprous oxide. The electrodes were modified by electropolymerization of lignin and subsequent pulse electrodeposition of Cu_2O. Characterization of the electrodes was performed by SEM microscopy; Raman; IR-ATR; and UV-visible spectroscopies, as well as electrochemical methods. Lignin films provide a micro-environment where Cu_2O is stabilized and also its reactivity is modified toward C-H-O containing compounds. The main products obtained from the reduction of CO_2 are formaldehyde, methyl formate and ethyl acetate, as detected and quantified by nuclear magnetic resonance and UV-Vis spectroscopy. Our results demonstrate that lignin is a good material for the formation and support of the electrodeposited Cu_2O, where the Cu_2O enables the potential use of solar energy for the photoelectrochemical reduction of CO_2 at low overpotentials.

Introduction

In the last two decades, the different entities responsible for the study and mitigation of climate change have focused on the rapid and constant increase of atmospheric carbon dioxide associated with global warming [1]. The earth's climate has warmed by about 0.6 ° C in the last 100 years,[2] which coincides with atmospheric CO_2 increasing by more than 60 ppm since it was first recorded in 1958 [3]. The direct relationship between the increase in global temperature and the concentration of CO_2 has affected, is affecting and irreproachably is affecting ecological systems and biota that are highly sensitive to ecological variables like temperature and precipitation [4–6].

At present, the atmospheric CO_2 concentration has exceeded the 400 ppm barrier, a value that had never before been recorded [7]. To mitigate the CO_2 increase, efforts are focused on enhancing energy efficiency and improving technologies for capture, storage and transformation of CO_2. Differents methods have been used for CO_2 transformation, among them, electrochemical and photoelectrochemical reduction are versatile methods that can be done under ambient conditions. In this context several metallic electrodes like, Pt, Ni, Cr and Mo, among others,[8,9] have been used to reduce CO_2 electrochemically, producing mainly C_1 compounds like CO or $HCOO^-$ [10–12]. The main problem is the high electrochemical overpotential required to reduce CO_2. Because CO_2 is stable and chemically inert, the single-electron reduction of CO_2 to an anion radical $CO_2^{\cdot-}$ requires a significant negative electro-chemical potential of -1.9 V vs NHE [13]. On the other hand, photoelectrochemical studies show decreased overpotential for CO_2 reduction.

Electrodes modified with a metal oxide semiconductor allow one to take advantage of semiconductor properties and to create the charge carriers using the eletrons from the conduction band to reduce the CO_2. A disadvantage of semiconductor materials is that the electron-hole separation gives rise to other processes, such as oxidation of the electrode or recombination of the photogeneratred carriers, that may occur and decrease system efficiency[14]

Metal oxide semiconductors have been used for CO_2 reduction, such as TiO_2[15,16], WO_3[17,18], ZnO[19,20], CdS[21,22], CdTe[23], and Cu_2O[24,25]. TiO_2 is the most widely used, but an important limitation of this semiconductor is the requirement of UV photons with wavelengths shorter than 380 nm to create electron-hole pairs [26]. This wavelength range impedes the use of the solar spectrum in more applied devices.

Cuprous oxide, Cu_2O, is another semiconductor that has attracted great interest. In contrast to TiO_2, Cu_2O has a high absorption coefficient[27] across the solar spectrum that allows it to photogenerate electron-hole pairs. Furthermore, Cu_2O has a conduction band edge positions that lies at a very negative potential, translating into high reducing power for the

[a] Pontificia Universidad Católica de Chile. Facultad de Química. Departamento de Química Inorgánica.
[b] University of Notre Dame, Department of Chemistry and Biochemistry, Notre Dame, Indiana 46556, United States.
[c] Department of Chemistry and Biochemistry, The Ohio State University, Columbus, OH 43210, USA.
[d] Pontificia Universidad Católica de Valparaíso, Facultad de Ciencias, Instituto de Química, Avda. Universidad 330, Valparaíso, Chile.
[e] Centro de Investigación en Nanotecnología y Materiales Avanzados, Pontificia Universidad Católica de Chile.
[f] UC-Energy Research Center.

Electronic Supplementary Information (ESI) available: Cyclic voltammetry of glassy carbon activation; cyclic voltammetry of the lignin-modified electrodes in acid solution; HNMR spectrum of samples; standard curves for products quantification; SEM image of the lignin-modified electrodes. See DOI: 10.1039/x0xx00000x

photogenerated electrons[28]. Cu_2O is a semiconductor that is easy to prepare and is composed of two very abundant and non-toxic elements[29]. It has been reported with a direct band gap near to 2.2 eV[30], and depending on doping level may have a n-type or p-type character. In recent works, Cu_2O has been used as a photocathode for photoelectrochemical reduction of CO_2[31–34]. Using a hybrid CuO/Cu_2O semiconductor K. Rajeshwar *et al* [28] reported the photo-electroreduction of CO_2 to methanol in aqueous solution by applying -0.2V vs NHE under simulated AM 1.5 solar irradiation. Also, using the Cu/Cu_2O system and applying high overpotential the reaction yields CH_4 and C_2H_4 as the main products [35]. However, the main drawback in the use of this semiconductor as a photocathode is its instability in aqueous solution resulting from the redox potentials of cuprous oxide lying within its own bandgap[36].

Then, to protect the electrode in aqueous solution A. Paracchino *et al.* covered Cu_2O with ZnO:Al, Ti_2O and Ag nanopaticles. Their results showed that the electrodes produced photocurrents of up to −7.6 mA cm^{-2} at a potential of 0V vs RHE and remained active after 1 hour of testing[36].

On the other hand, lignin is a biopolymer present in plants, which constitutes the cell wall along with cellulose and hemicellulose. In the paper industry lignin is a byproduct from the treatment lignocellulosic material[37] . Lignin is a very abundant biopolymer in nature, which is environmentally benign, sustainable, biodegradable and low cost[38].

The typical structure of lignin consists of three basic monomer units; coumaryl alcohol, coniferyl alcohol and sinapyl alcohol. It has a random organization, with C-O and C-C linkages. The common functional groups in lignin include methoxyl, phenolic hydroxyl, aliphatic hydroxyl and carbonyl groups[39]. In recent works, lignin has been used in different applications, such as lithium ion batteries[40–42], stabilization of nanoparticles[43–46], hydrogen production[47] and H_2O_2 generation[48] among others.

It is also possible for lignin-modified electrodes to be used for electrocatalytic applications. G. Milczareck reported electrodes modified with lignin[49] are useful for the reduction of acidic nitrite[50]. Operating at 0.0V vs Ag/AgCl, lignin-modified electrodes could detect nitrite at concetrations between 1 to 250 µM. Furthermore, lignin- modified electrodes oxidized NADH. The redox activity of lignosulfonate shows persistent catalytic activity for the electrooxidation of NADH[51].

To the best of our knowledge, the use of lignin as a supporting material for the modification of electrodes with Cu_2O has not been reported. This work investigates glassy carbon electrodes modified with lignin and cuprous oxide (GC-LS-Cu_2O) and glassy carbon electrodes modified with Cu_2O (GC-Cu_2O). We report the characterization and use of these modified electrodes for the photoelectroreduction of CO_2. Our results indicate that GC-LS-Cu_2O electrodes show better photo-stability than GC-Cu_2O in aqueous solution obtaining formaldehyde, methyl formate and ethyl acetate as reduction products at low overpotentials.

Experimental

Electrochemical experiments

All electrochemical experiments were carried out using a three-electrode system with a glassy carbon electrode as working electrode, a platinum wire counter electrode and a Ag/AgCl (saturated KCl) reference electrode.

Glassy carbon activation and electrochemical deposition of lignin

Prior to electrode modification, 3mm diameter glassy carbon electrodes (model CHI104, CH Instruments) for cyclic voltammetry and glassy carbon plate (SPI-Glas 11 grade, SPI supplies) of 1.18 cm^2 for electrolysis or characterization were polished with alumina powders decreasing in size from 1.0 µm to 0.3 µm and 0.1 µm, then rinsed with milli-Q water (18 MΩ cm^{-1}), sonicated for 5 minutes in acetone and rinsed again with milli-Q water. Activation of the glassy carbon electrode was done by cyclic voltammetry in a phosphate buffer (pH = 7.4), performing 15 continuous cycles at a scan rate of 100 mVs^{-1} in a potential window from -0.2 to 1.7V vs Ag/AgCl (sat. KCl) [51] (Figure S1, ESI†).

For the polymerization process the activated electrode was placed vertically and 50 uL of a 0.5 mg/mL solution of sodium lignosulfonate and 0.5 M H_2SO_4 was added and left standing for 20 minutes, then the electrode was carefully rinsed with water and immersed in a solution consisting of 0.25 mg / mL lignin and 0.5M H_2SO_4. The lignin was electropolymerized by cycling the potential between -0.6 V and 1.0 V vs Ag/AgCl at a scan rate of 100 mVs^{-1} for 20 continuous cycles[50].

Electrodeposition of Cu_2O

Cu_2O particles were pulse deposited at 50% duty cycle at 5 Hz with a pulse-on time of 100 ms and a total reaction time of 30 minutes. The pulse potential varied between -0.4V and -0.35V vs Ag/AgCl. The pulse electrodeposition method was done in a copper-citrate solution with 0.05M $CuSO_4{\cdot}5H_2O$ and 0.1M sodium citrate. The pH was adjusted to pH = 12.50 by additions of 4M NaOH aliquots[52].

CO_2 reduction

The photoelectrochemical experiments and controlled potential electrolysis were carried out in a 0.1M Na_2SO_4 and CO_2 saturated solution in a homemade three compartments electrochemical cell with a window quartz, where the catholyte is separate from anolyte by a glass frit. Irradiation was carried out using a 500 W Xe–Hg Lamp (Oriel Corporation) light source. The reaction products were detected by nuclear magnetic resonance and gas chromatography and UV-Vis spectroscopy.

H^1NMR experiments were carried out following the method reported by Thomas F. Jaramillo et al [53]. Where, a water suppression program was used to decrease the H_2O signal interfering with H^+ from reaction products.

Spectroscopic and Morphological characterization

The IR spectrum of GC-LS was obtained using a Nicolet iS10 FTIR-ATR spectrophotometer. The crystalline structure of the modified electrodes was determined by X-ray diffraction (XRD) with a Bruker D8 advance diffractometer. Raman spectrum and AFM images were carried out using a WiTec Alpha 300 RA Raman-AFM. SEM images were obtained with a Quanta 250 FEG scanning electron microscope.

In several experiments, the same sample was used for Raman, AFM and SEM characterization. Using the 532 nm laser source, a specific area was marked. Afterward this mark was easily identified in the SEM or AFM microscope allowing correlation between the SEM image and other measurements.

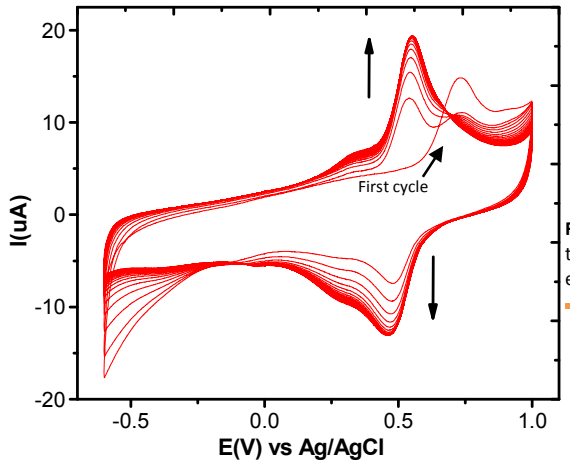

Figure 1: Cyclic voltammetry of the lignin electropolymerization process on the glassy carbon electrode in 0.05 M lignosulfonic acid and 0.1M sulfuric acid electrolyte solutions.

Results and discussion

Lignin was electropolymerized on glassy carbon electrode between -0.6 and 1.0 V vs Ag/AgCl in a 0.05 M lignosulfonic acid and 0.1M sulfuric acid solutions at a scan rate of 100 mV/s for 20 continuous cycles. The cyclic voltammogram in Figure 1 shows the electropolymerization process. An irreversible oxidation peak is observed initially at 0.72V, but in subsequent scans a reversible redox pair at ca. 0.5V appears. These processes are assigned to the irreversible oxidation of the methoxy groups and the quinone-hydroquinone redox couple, respectively[51].

The quinone-hydroquinone redox couple does not disappear when the electrode is transferred to a Lignin-free solution, showing the efficient electrode modification (Figure S2, ESI†). The maximum surface coverage of lignin was calculated using the following relationship (1)[54]:

$$\Gamma = Q / nFA \quad (1)$$

Where *Q* is the charge consumed during the cyclic voltammetry, *n* is the numbers of electrons transferred in the redox process, F is Faraday's constant and A is electrode area (cm^2). From Eq. 1, a surface coverage of $1*10^{-9}$ $molcm^{-2}$ is determined, which corresponds to multilayers of lignin films over the glassy carbon electrode.

The presence of sulfonate groups in the lignin can be observed by FT-IR ATR spectroscopy. Figure 2 shows the FT-IR ATR spectra of lignin samples. For comparison, Figure 2(a) shows the FTIR typical of powdered lignin. Figure 2(b) displays peaks characteristic of the lignin on the GC electrode with a wide band at 1210 cm^{-1} and another band at 1028 cm^{-1} that can be assigned to the stretching of O=S=O and SO_3^-H stretching in SO_3H groups, respectively[55,56]. Other characteristic vibrations of lignin are observed, such as the C=C stretching (1593 cm^{-1} and 1507 cm^{-1}) from benzene structures and aromatic and aliphatic hydroxyl groups (ca. 3550 cm^{-1})[56,57].

Cu_2O was formed on the lignin-modified electrode by pulse electrodeposition, generating the final modified electrode. As a control measurement a bare glassy carbon electrode was modified in the same way and then used to compare the observed

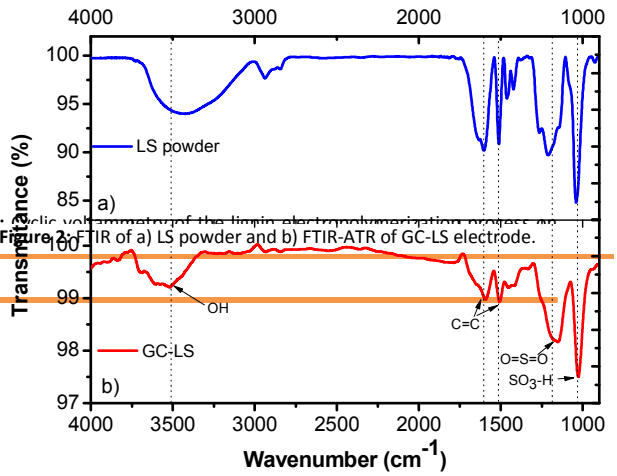

Figure 2: FTIR of a) LS powder and b) FTIR-ATR of GC-LS electrode.

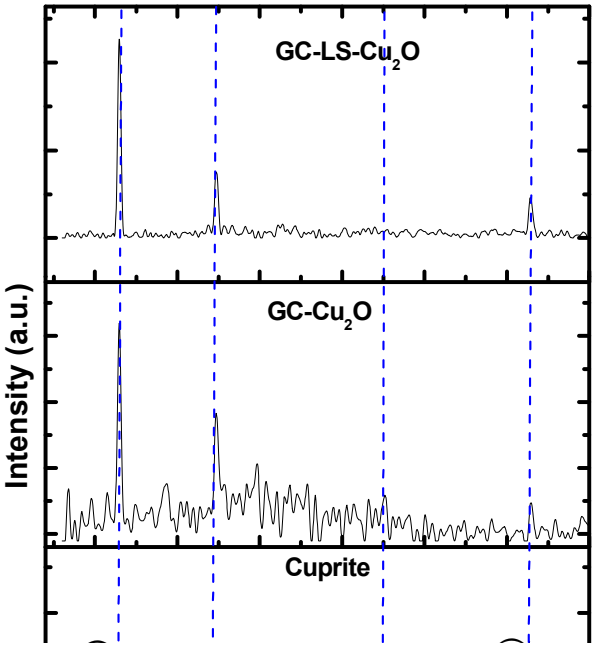

Figure 3: XRD pattern of GC-LS-Cu_2O and GC-Cu_2O electrodes. The database reference lines for cuprite are shown.

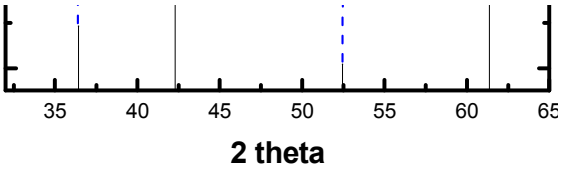

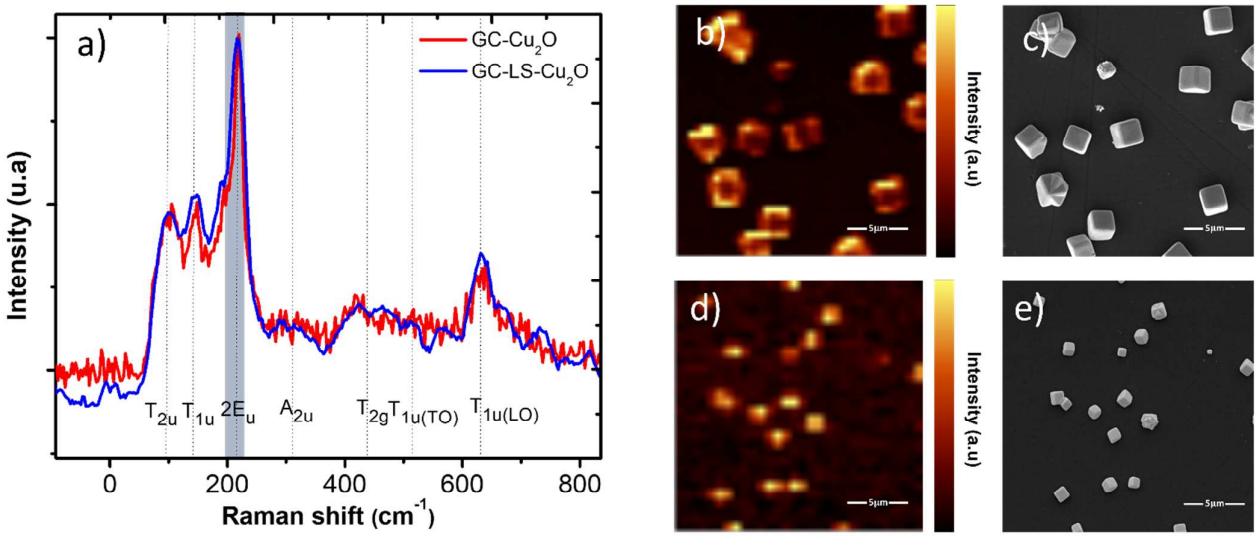

Figure 4: Raman spectra, 2D Raman map and SEM images of GC-LS-Cu_2O (blue line in spectra (a), (b) and (c) images respectively) and GC-Cu_2O electrodes (red line in spectra (a), (d) and (e) images respectively). The Marc in the vibrational mode $2E_u$ correspond to filter to maximum intensity of 2D map of GC-LS-Cu_2O and GC-Cu_2O.

characterization and electrochemical properties.

X-ray diffraction spectroscopy was used to determine the crystal structure of the semiconductor. Figure 3 shows the diffraction patterns observed from GC-Cu_2O and GC-LS-Cu_2O. The observed peaks correspond to the Miller indices (111), (200), and (220) for a face centered cubic structure, which are consistent with the presence of cuprite as the main species on the electrodes[58].

Raman spectroscopy was performed to further investigate the chemical nature of modified electrodes. Raman spectra from the GC-LS-Cu_2O and GC-Cu_2O were obtained with 532 nm laser irradiation. The Raman spectrum of the electrodes (Figure 4(a)) show characteristic vibrational modes of Cu_2O with A, E, and T symmetry in the region between 100 and 700 cm^{-1}. The observed Raman shifts are assigned as follows: 105 cm^{-1} (T2u), 156 cm^{-1} (T1u),227 cm^{-1} (2Eu), 322 cm^{-1} (A2u), 430 cm^{-1} (T2g), 517 cm^{-1} (T1u(TO)) and 639 cm^{-1} (T1u(LO)) [59] . Also, in both electrodes, Cu_2O shows a broad peak near 3000 cm^{-1} (not shown) which has been character. The observed Raman bands are associated with copper vacancies interactions that lead to p-type conductivity.[65] and are consistent with previous reports[59]. n-type semiconductors arise from oxygen vacancies that are not pronounced in our spectra.

The surface morphology of electrodes also was characterized by AFM and FE-SEM microscopy. The AFM images in Figures 5 show the 2D, 3D and cross-sectional surface of GC-LS-Cu_2O (5(a), 5(b) and 5(c), respectively) and GC-Cu_2O (5(d), 5(e) and 5(f), respectively) electrodes. Both electrodes show well-dispersed cuprous oxide particles on the surface; however, the particles grew to at least

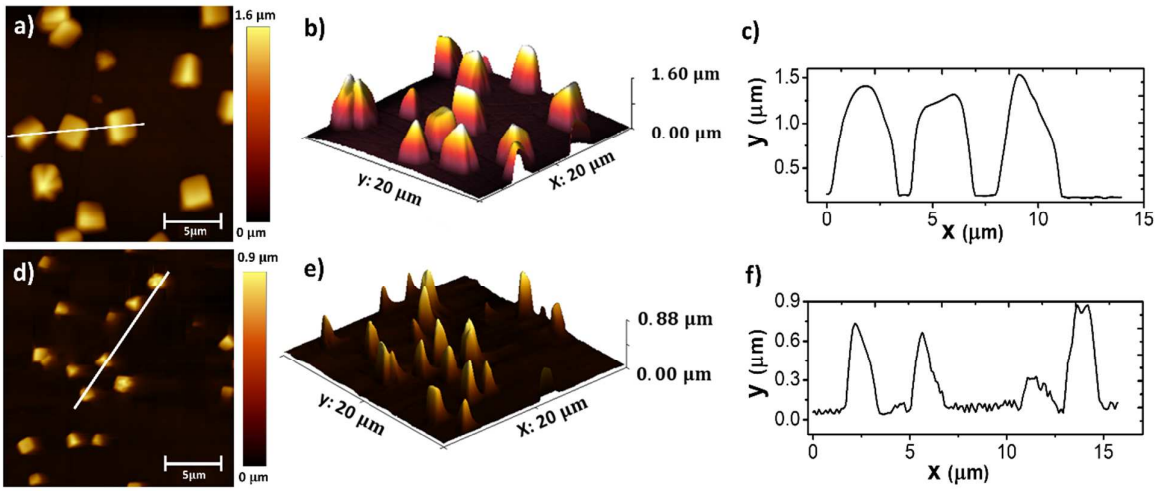

Figure 5: 2D and 3D AFM images of (a,b) GC-LS-Cu_2O and (d,e) GC-Cu_2O. (c,f) Cross-section analysis of 2D AFM images of GC-LS-Cu_2O and GC-Cu_2O.

previously assigned to photoluminescence that arises when the semiconductor is irradiated with a 532 nm laser[60–62]. On the GC-LS-Cu_2O electrode, areas associated with lignin exhibited a large fluorescence signal and Raman scattering was not detectable, using either 532nm or 785nm laser excitation. Thus, the lignin structure was not possible to identify because of the fluorescence. Additionally, extended exposure to the laser can burn the lignin. Other work has used a 1064 nm laser to reduce the fluorescence on this polymer and thus identify the characteristic signals[63].

Cu_2O has a larger Raman cross-section than the substrate or lignin, which allows one to discriminate the semiconductor from the substrate (glassy carbon) and the lignin in a 2D Raman map. The 2D images of the Figure 4(b) and 4(d) correspond to a 20 µm x 20 µm region, mapped by the intensity in gray band that corresponds to the 2Eu vibrational mode of Cu_2O[64] and is inidicative of Cu defects[59]. The features arising from GC-Cu_2O and LS-Cu_2O in the Raman map, correlate well with the AFM (Figure 5) and SEM images (Figure 4(c)) and 4(e). The Raman spectrum of Cu_2O reveals p-type twice the size on electrodes modified with lignin than on GC-Cu_2O, as is evident in the cross-sectional profile analysis of the electrodes. The increased size of the GC-LS-Cu_2O may occur due to the more hydrophilic microenvironment. The lignosulfonate used presents various hydrophobic phenylpropanoid residues, but also presents hydrophilic groups like aromatic and aliphatic hydroxyl groups and sulfonates groups that can provide hydrophilic zones with a propitious environment for the Cu_2O to grow. In related work, Li et al synthesized ZnO with the assistance of sodium lignosulfonate and proposed a mechanism for ZnO growth where a synergistic effect between the lignosulfonate aggregation shape and polar ZnO crystals[66] . SEM images verified that the morphology of GC-LS-Cu_2O and GC-Cu_2O electrodes correspond to well disperse cuprous oxide cubic particles on the surface of electrodes. The SEM images in the Figure 4(c) and 4(e) show the particles measured in the same area that AFM images were recorded. EDX analysis reports the presence of copper, oxygen, sulfur and carbon on GC-LS-Cu_2O electrodes and copper and oxygen in GC-Cu_2O electrodes (Not shown). SEM image of GC-LS showed well disperse lignin on the surface of electrodes (Figure S6, ESI†).

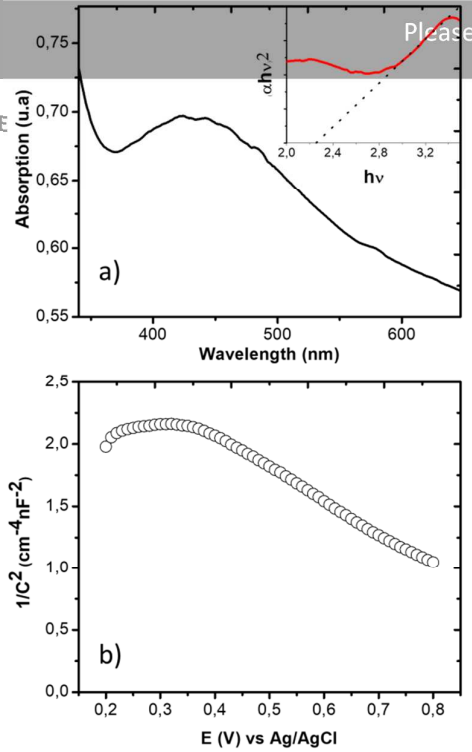

Figure 8: Linear sweep voltammetry of GC-LS, GC-LS-Cu_2O and GC-Cu_2O electrodes carried out in 0.1M sodium sulfate saturated with CO_2 and under visible light irradiation (100 mW cm^{-2}). Scan rate = 10 mVs^{-1}

The semiconductor band-gap of Cu_2O was further determined using UV-Vis spectroscopy. Figure 6(a) shows the maximum absorbance of Cu_2O and the inset plots the intersection of the straight-line fit of the linear regime of the Tauc plot derived from UV-Vis. The bandgap energy values (Eg) of the semiconductor films were determined from transmittance spectra using Tauc relation in (Equation (2)):

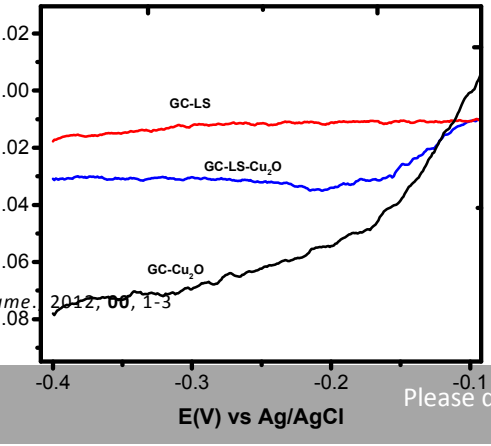

Figure 6: (a) UV-Vis absorption spectra obtained of an ITO modified electrode with Cu_2O. Inset, Tauc's plot of Cu_2O electrodeposited by pulse electrodeposition. (b) Mott-Schottky plot of Cu_2O carried out in a 0.1M buffer borate solution.

$$\alpha h\vartheta = A(h\vartheta - E_g) \quad (2)$$

Where A is a constant, $h\vartheta$ is the photon energy, α is the absorption coefficient, and *n* depends on the nature of the transition. For direct allowed transitions, *n* = ½[67]. Therefore, in a plot of $(\alpha h\nu)^2$ vs $h\vartheta$, the Eg value can be found by extrapolating the linear portion of the plot to the energy axis at α = 0 [68], as shown in the inset in figure 6 (a). From the linear fit, an Eg value of 2.28 eV has been obtained that
agrees well with those reported in the literature for the Cu_2O phase[69].

Mott-Schottky analysis is based on the assumption that the capacitance of the space charge layer is much less than that of the Helmholtz layer[70]. Mott-Schottky relationship on p-type

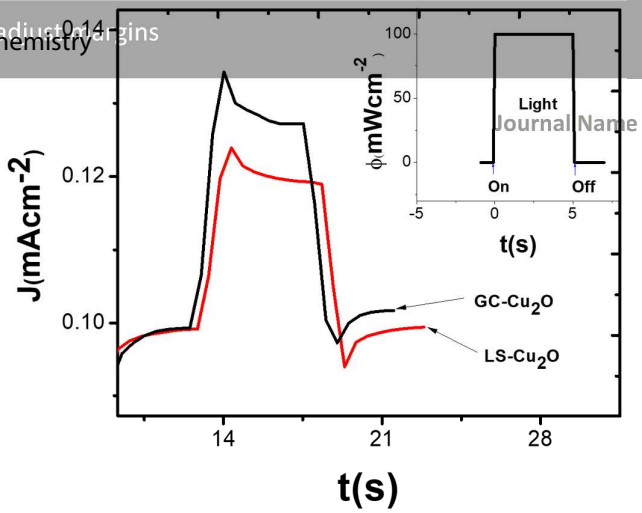

Figure 7: Photocurrent transient of LS-Cu_2O (red) and GC-Cu_2O (black) modified electrodes in a 0.1M sodium sulfate solution saturated with CO_2 and applying -0.4V vs Ag/AgCl. Inset: Light pulse waveform for current transient measurements.

semiconductor is expressed according to the Mott Schottky equation (3):

$$\frac{1}{C^2} = \left(\frac{2}{\varepsilon \cdot \varepsilon_0 \cdot N_D^2}\right) \cdot \left(V - V_{FB} - \frac{kT}{e}\right) \quad (3)$$

Where ε is the dielectric constant of Cu_2O (ε = 6.3)[44], ε_0 is the permittivity of vacuum (8.854 × 10^{-12} F m^{-1}), N_D is the donor density, which is calculated from the slope of the curve, *e* is the electronic charge (1.603 × 10^{-19} C), *T* is the operation temperature (298 K), and *k* is the Boltzmann constant (1.38×10^{-23} J K^{-1}). *V* is the electrode potential, V_{FB} is the flat band potential, and *C* is the depletion-layer capacitance. The Mott-Schottky plot of the Cu_2O film are shown in Figure 6(b). There is a positive slope in the linear region of the plot, indicating a p-type characteristic according to Equation 3. The carrier donor concentration (N_D) calculated from the Mott-Schottky analysis was 8.1 x 10^{21} cm^{-3} and the flat band potential extrapolation of the straight line corresponds to 1.15 V vs Ag/AgCl. The apparent donor carrier concentration is higher than expected; however, polycrystalline Cu_2O can contain grain boundaries and surface sites that can increase the number of defects in its structure[59]. The p-type character obtained from Mott-Schottky equation is consistent with photocurrent transient for CO_2 reduction shown in the Figure 7 and the Raman results.

The photoelectrochemical response of GC-LS-Cu_2O shows that the recombination process of photoexcited electron-hole pairs occurs at lower energy than for GC-Cu_2O. F. Herrera et al.[71] reported that the steady-state photocurrent ($\mathbf{I_{ph-st}}$) can be related to the maximum photocurrent ($\mathbf{I_{ph-on}}$) achieved at time zero, or initial pulse time, and the current associated with the recombination processes ($\mathbf{I_{ph-R}}$) according to equation 4:

Compound	CO_2 reduction products		standards	
Water	s	4.79	s	4.79[51]
DMSO	s	2.76	s	2.6[51]
Phenol	t	7.36	t	7.2[51]
	t	7.02	t	6.86[51]
	d	6.96	d	6.8[51]
methyl formate	s	8.73	s	8.71
	s	3.91	s	3.76
Ethyl acetate	q	4.25	q	4.14[69]
	s	2.27	s	2.07[69]
	t	1.52	t	1.24[69]

Table 1: Reaction product signals compared with standards obtained in aqueous solution.

$$I_{ph-st}/I_{ph-on} = 1-(I_{ph-R}/I_{ph-on}) \quad (4)$$

Thus, when I_{ph-R} decreases, the transient ratio between steady-state and the maximum of photocurrent increases to 1, where recombination processes disappear. The pulse photocurrent transient in Figure 7 results from a square wave chopped light excitation, and compares the transient between a GC-LS-Cu_2O electrode and a GC-Cu_2O electrode in a 0.1M sodium sulfate saturate with CO_2 applying -0.4V vs. Ag/AgCl. A larger current density is observed in the GC-Cu_2O electrode compared to GC-LS-Cu_2O according to linear sweep voltammetry experiments (Figure 8). This difference in photocurrent may arise from the lignin support material hampering the charge transfer at the electrode; however, the most important feature is less recombination is observed when lignin is used as support material. Acording to equation 4, While GC-Cu_2O shows a maximum of photocurrent (R) of 0.81, GC-LS-Cu_2O shows a maximum of 0.92 that exhibits the best R value close to 1. This indicates that when we use a GC-LS-Cu_2O the electron-hole recombination decreases compared to GC-Cu_2O. This result suggest that, in the presence of lignin, the sulfonate and hydroxyl groups may act like commonly used electron-hole scavengers, impeding the recombination process of the charge carriers [72–74].

The CO_2 photoelectrochemical reduction was performed by controlled potential electrolysis applying -0.4V vs Ag/AgCl over 4 hours. The applied overpotential was selected according to the stability of Cu_2O . At potentials greater than -0.4V it is possible to find Cu (0) that interferes with electrocatalysis. The reaction products were detected and quantified by nuclear magnetic resonance, UV-Vis spectroscopy, and gas chromatography, where gaseous products were not detected.

Table 1 summarizes and assigns the signals of H^1NMR for observed CO_2 reduction products and internal standards, such as phenol and DMSO. The reaction products identified were ethyl acetate and methyl formate (Figure S3, ESI†), which was corroborated by comparisons with a database of standards. Also, using UV-Vis spectroscopy with chromotropic acid method[75], formaldehyde was detected (Figure S8, ESI†). The amounts of product detected, analytical methodology used and faradaic efficiency are summarized in Table 2.

Electrode	Compound	Concentration (ppm)	Method detection	Faradaic efficiency (%)
GC-LS-Cu_2O	Ethyl acetate	172	H^1RMN	37.60
	Methyl formate	250	H^1RMN	32.11
	Formaldehyde	0.43	Chromotropic acid method	0.05
GC-Cu_2O GC-LS GC	Reaction products were not detected			

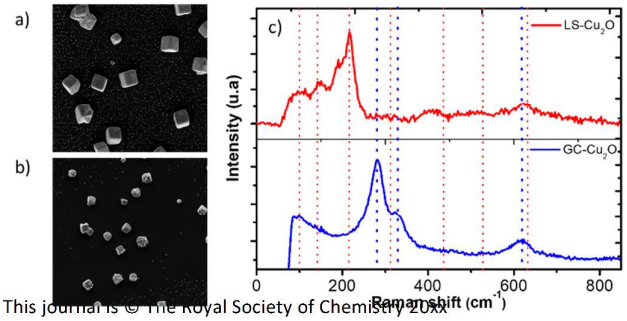

It is worth mentioning that the electrochemical reaction in the absence of light at the overpotential studied did not generate reaction products using either the GC, GC-LS or GC-Cu_2O electrodes.

Stability test

After electrolysis, SEM images and Raman spectra were recorded to identify significant changes in the structure and chemical nature of both electrodes.

The SEM image in Figure 9(a) for GC-LS-Cu_2O shows the morphology of the cubic Cu_2O is maintained, with little grains in the surface of electrodes from the sodium sulfate solution. In contrast, Figure 9 (b) shows the GC/Cu_2O electrode is deformed from the initial structure, probably due to photocorrosion processes[30]. A Raman spectrum of different zones of GC-Cu_2O shows mainly the presence of CuO, in agreement with previous reports for an unprotected electrode.[36] Raman spectra of GC-Cu_2O, Figure 9(c), shows three characteristic vibrational modes with Raman shifts of 282 cm^{-1} (A_g), 324 cm^{-1} (B_g) and 617 cm^{-1} (B_g), consistent with CuO [76]. On the other hand, the post-electrolysis Raman analysis of GC-LS-Cu_2O electrode continues to show features of Cu_2O particles quite similar to those presented in Figure 4(c). This indicates the chemical nature of the semiconductor remains constant and does not photodegrade, which is consistent with the morphology observed in Figure 9. These results, together with the photocurrent studies, show that the system where lignin is used as a support material is better compared to a system devoid of the biopolymer. We believe that this is due to the mechanism described above regarding the generation of a microenvironment that, in addition to allowing a greater growth of the semiconductor in specific zones, reduces the recombination processes, where the hydrophilic groups on lignin act as scavegers of the photogenerated holes that can oxidize Cu (I) to Cu (0).

Conclusions

In this work, it was demonstrated the synthesis of Cu_2O semiconductor particles using lignin as a support material. GC-LS-Cu_2O were synthetized by pulse electrodeposition and fully characterized. This electrode was capable of reducing carbon dioxide to formaldehyde, methyl formate and ethyl acetate applying a very low overpotential (-0.4 V vs Ag/AgCl). While Cu_2O has appeared as a good candidate for photo-electrochemical applications, due to its semiconductor properties, low stability has been a challenge for the extensive use of this material. Our results indicate a lignin film provides a specific microenvironment that is able to photo-stabilize Cu_2O. This result offers new uses for this biopolymer, which is underrated and is mainly used for thermal energy generation in cellulose mills. The as designed electrode further demonstrates a new concept in the use of biomass and an abundant, low toxicity transition metal for photo-electrocatalysis in CO_2 transformation.

Acknowledgements

This work was supported by Project RC 130006, CILIS, granted by Fondo de Innovación para la Competitividad, del Ministerio de Economia, Fomento y Turismo, Chile, and FONDECYT 1141199, 3160217 and 1160485, CONICYT 21130214 grant. FONDEQUIP programs EQM150101 and EQM150020. A National Science Foundation award CHE-1507287 to ZDS is also acknowledged. Pontificia Universidad Católica de Chile, facultad de química, departamento de química inorgánica.

Notes and references

Figure 9: SEM images of (a)LS-Cu2O and (b) GC-Cu2O and (c)Raman spectrum of electrodes after electrolysis**.**

1 A. N. Grace, S. Y. Choi, M. Vinoba, M. Bhagiyalakshmi, D. H. Chu, Y. Yoon, S. C. Nam and S. K. Jeong, *Appl. Energy*, 2014, **120**, 85–94.

2 G. Walther, E. Post, P. Convey, A. Menzel, C. Parmesan, J. Beebee, Trevor J C. Fromentin, O. Hoegh-guldberg and F. Bairlein, *Nature*, 2002, **416**, 389–395.

3 C. D. Keeling, *Annu. Rev. Energy Env.*, 1998, **23**, 25–82.

4 IPCC – Intergovernmental Panel on Climate Change, Climate Change 2013. The Physical Science Basis. Fifth Assessment Report, Cambridge University Press, United Kingdom, 2013.

5 T. L. Root, J. T. Price, K. R. Hall, S. H. Schneider, C. Rosenzweig and J. A. Pounds, *Nature*, 2003, **421**, 57–60.

6 H. Feuchtmayr, R. Moran, K. Hatton, L. Connor, T. Heyes, B. Moss, I. Harvey and D. Atkinson, *J. Appl. Ecol.*, 2009, **46**, 713–723.

7 J. P. Howe, *Environ. Hist. Durh. N. C.*, 2015, **20**, 286–293.

8 Y. Hori, *Mod. Asp. Electrochem.*, 2008, 89–189.

9 T. Smolinka, M. Heinen, Y. X. Chen, Z. Jusys, W. Lehnert and R. J. Behm, *Electrochim. Acta*, 2005, **50**, 5189–5199.

10 Q. Shen, Z. Chen, X. Huang, M. Liu and G. Zhao, *Environ. Sci. Technol.*, 2015, **49**, 5828–5835.

11 Q. Shen, X. Huang, J. Liu, C. Guo and G. Zhao, *Appl. Catal. B, Environ.*, 2017, **201**, 70–76.

12 X. Huang, Q. Shen, J. Liu and G. Zhao, *Energy Environ. Sci.*, 2016, **9**, 3161–3171.

13 S. N. Habisreutinger, L. Schmidt-mende and J. K. Stolarczyk, *Angew. Chemie Int. Ed.*, 2013, **52**, 7372–7408.

14 J. Liu, H. Shi, Q. Shen, C. Guo and G. Zhao, *Green Chem.*, 2017, **19**, 5900–5910.

15 H. Abdullaha, M. M. R. Khan, H. R. Ong and Z. Yaakob, *J. CO2 Util.*, 2017, **22**, 15–32.

16 H. Yu, S. Yan, P. Zhou and Z. Zou, *Appl. Surf. Sci.*, 2018, **427**, 603–607.

17 Y. Yang, F. Zhan, H. Li, W. Liu and S. Yu, *J. Solid State Electrochem.*, 2017, 2231–2240.

18 M. A. Gondal, M. A. Dastageer, L. E. Oloore and U. Baig, *J. Photochem. Photobiol. A Chem.*, 2017, **343**, 40–50.

19 K. Deng, B. Hu, Q. Lu and X. Hong, *Catal. Comun.*, 2017, **100**, 81–84.

20 X. Jiang, F. Cai, D. Gao, J. Dong, S. Miao, G. Wang and X. Bao, *Electrochem. commun.*, 2016, **68**, 67–70.

21 M. F. Kuehnel, D. W. Wakerley, K. L. Orchard and E. Reisner, *Angew. Chemie Int. Ed.*, 2015, **54**, 9627–9631.

22 Y. S. Chaudhary, T. W. Woolerton, C. S. Allen, J. H. Warner, E. Pierce, S. W. Ragsdale and F. A. Armstrong, *Chem. Commun*, 2012, **48**, 58–60.

23 D. Guzmán, M. Isaacs, I. Osorio-Román, M. García, J. Astudillo and M. Ohlbaum, *ACS Appl. Mater. Interfaces*, 2015, **7**, 19865–19869.

24 R. A. Geioushy, M. M. Khaled, K. Alhooshani, A. S. Hakeem and A. Rinaldi, *Electrochim. Acta*, 2017, **245**, 456–462.

25 R. A. Geioushy, M. M. Khaled, A. S. Hakeem, K. Alhooshani and C. Basheer, *J. Electroanal. Chem.*, 2017, **785**, 138–143.

26 N. Sergio, D. Amarajothi, Á. Mercedes and G. Hermenegildo, *ChemSusChem*, 2013, **6**, 562–577.

27 R. Wick and S. D. Tilley, *J. Phys. Chem. C*, 2015, **119**, 26243–26257.

28 G. Ghadimkhani, N. R. de Tacconi, W. Chanmanee, C. Janakyab and K. Rajeshwar, *Chem. Commun*, 2013, **49**, 1297–1299.

29 H. A. Al-Jawhari, *Mater. Sci. Semicond. Process.*, 2015, **40**, 241–252.

30 J. Tu, Y. Yuan, H. Jiao and S. Jiao, *RSC Adv.*, 2014, **4**, 16380–16384.

31 T. Chang, R. Liang, P. Wu, J. Chen and Y. Hsieh, *Mater. Lett.*, 2009, **63**, 1001–1003.

32 J. Bugayong and G. L. Griffin, *ECS Trans.*, 2013, **58**, 81–89.

33 J. Qiao, M. Fan, Y. Fu, Z. Bai, C. Ma, Y. Liu and X.-D. Zhou, *Electrochim. Acta*, 2015, **153**, 559–565.

34 M. Schreier, P. Gao, M. T. Mayer, J. Luo, T. Moehl, M. K. Nazeeruddin, S. D. Tilley and M. Gratzel, *Energy Environ. Sci.*, 2015, **8**, 855–861.

35 X. Ba, L.-L. Yan, S. Huang, J. Yu, X.-J. Xia and Y. Yu, *J. Phys. Chem. C*, 2014, **118**, 24467–24478.

36 A. Paracchino, V. Laporte, K. Sivula, M. Grätzel and E. Thimsen, *Nat. Mater.*, 2011, **10**, 456–461.

37 W. Ye, X. Li, J. Luo, X. Wang and R. Sun, *Ind. Crop. Prod.*, 2017, **109**, 410–419.

38 M. Uddin, P. K. Alaboina, L. Zhang and S. Cho, *Mater. Sci. Enginnering B*, 2017, **223**, 84–90.

39 H. Chung and N. R. Washburn, *Green Mater.*, 2012, **1**, 137–160.

40 W. Zhanga, J. Yin, Z. Lin, H. Lin, H. Lu, Y. Wang and W. Huang, *Electrochim. Acta*, 2015, **176**, 1136–1142.

41 Z. Wang, W. He, X. Zhang, Y. Yue, G. Yang, X. Yi, Y. Wang and J. Wang, *ChemElectroChem*, 2017, **4**, 671–678.

42 V. Garcia-Negron, N. D. Phillip, J. Li, C. Daniel, D. Wood, D. J. Keffer, O. Rios and D. P. Harper, *Energy Technol.*, 2017, **37996**, 1311–1321.

43 G. Milczarek, T. Rebis and J. Fabianska, *Colloids Surfaces B Biointerfaces*, 2013, **105**, 335–341.

44 G. Milczarek and A. Ciszewski, *Colloids Surfaces B Biointerfaces*, 2012, **90**, 53–57.

45 K. R. Aadil, A. Barapatre, A. S. Meena and H. Jha, *Int. J. Biol. Macromol.*, 2016, **82**, 39–47.

46 R. M. Buoro, R. P. Bacil, R. P. da Silva, L. C. C. da Silva, A. W. O. Lima, I. C. Cosentino and S. H. P. Serrano, *Electrochim. Acta*, 2013, **96**, 191–198.

47 T. Hibino, K. Kobayashi, M. Nagao and S. Teranishi, *ChemElectroChem*, 2017, **4**, 1–6.

48 H. Huang, C. Han, G. Wang and C. Feng, *Electrochim. Acta*, 2018, **259**, 637–646.

49 G. Milczarek, *Electroanalysis*, 2007, **19**, 1411–1414.

50 G. Milczarek, *Electroanalysis*, 2008, **20**, 211–214.

51 G. Milczarek, *Langmuir*, 2009, **25**, 10345–10353.

52 Y. Gu, X. Su, Y. Du and C. Wang, *Appl. Surf. Sci.*, 2010, **256**, 5862–5866.

53 K. P. Kuhl, E. R. Cave, D. N. Abram and T. F. Jaramillo, *Energy Environ. Sci.*, 2012, **5**, 7050–7059.

54 Y. Dessie and S. Admassie, *Orient. J. Chem.*, 2013, **29**, 1359–1369.

55 S. Li, N. Li, G. Li, L. Li, AiqinWang, Y. Cong, X. Wang and T. Zhang, *Green Chem.*, 2015, **17**, 3644–3652.

56 R. Shu, Y. Xu, L. Ma, Q. Zhang, T. Wang, P. Chen and Q. Wu, *RSC Adv.*, 2016, **6**, 88788–88796.

57 H. Xu, G. Yu, X. Mu, C. Zhang, P. DeRoussel, C. Liu, B. Li and H. Wang, *Ind. Crop. Prod.*, 2015, **76**, 638–646.

58 D. Osorio-Rivera, G. Torres-Delgado, J. Márquez-Marín, R. Castanedo-Pérez, M. A. Aguilar-Frutis and O. Zelaya-Ángel, *J. Mater. Sci. Mater. Electron.*, 2017, **29**, 851–857.

59 T. Sander, C. T. Reindl, M. Giar, B. Eifert, M. Heinemann, C. Heiliger and P. J. Klar, *Phys. Rev. b*, 2014, **90**, 45203.

60 M. Thoury, B. Mille, T. Séverin-Fabiani, L. Robbiola, M. Réfrégiers, J.-F. Jarrige and L. Bertrand, *Nat. Commun.*, 2016, **7**, 13356.

61 Y. Petroff, P. I. Yu and Y.R. Shen, *Phys. Rev. b*, 1975, **12**, 2488–2495.

62 J. Li, Z. Mei, D. Ye, H. Liang, L. Liu, Y. Liu, A. Galeckas, A. Y. Kuznetsov and X. Du, *Opt. Soc. Am.*, 2013, **3**, 2072–2077.

63 J. S. Lupoi, E. Gjersing and M. F. Davis, *Front. Bioeng. Biotechnol.*, 2015, **3**, 1–18.

64 A. Bhaumik, A. Haque, P. Karnati, M. F. N. Tau, R. Patel and K. Ghosh, *Thin Solid Films*, 2014, **572**, 126–133.

65 L. Xiong, S. Huang, X. Yang, M. Qiu, Z. Chen and Y. Yu, *Electrochim. Acta*, 2011, **56**, 2735–2739.

66 Y. Li, H. Zuo, Y. Guo, T. Miao and Q. Pan, *Nanoscale Res. Lett.*, 2016, **11**, 260.

67 S. Prabahar, V. Balasubramanian, N. Suryanarayanan and N. Muthukumarasamy, *Chalcogenide Lett.*, 2010, **7**, 49–58.

68 A. Burgos, R. S. Schrebler, H. Gómez, F. A. Cataño, R. E. Marotti and E. A. Dalchiele, *Int. J. Electrochem. Sci.*, 2015, **10**, 10543–10553.

69 P.Grez, F.Herrera, G.Riveros, R.Henríquez, A.Ramírez, E.Muñoz, E.A.Dalchiele, C.Celedón and R.Schrebler, *Mater. Lett.*, 2013, **92**, 413–416.

70 A. Burgos, F. Cataño, B. Marí, R. Schrebler and H. Gómez, *J. Electrochem. Soc.*, 2016, **163**, 562–567.

71 F. V. Herrera, P. Grez, R. Schrebler, L. A. Ballesteros, E. Muñoz, R. Córdova, H. Altamirano and E. A. Dalchiele, *J. Electrochem. Soc.*, 2010, **157**, D302–D308.

72 A. Cavicchioli and I. G. R. Gutz, *J. Braz. Chem. Soc.*, 2002, **13**, 441–448.

73 S. V. Kershaw, Lihong Jing, X. Huang, M. Gao and A. L. Rogach, *Mater. Horizons*, 2017, **4**, 155–205.

74 Y. Ma, S. R. Pendlebury, A. Reynal, F. Le Formal and J. R. Durrant, *Chem. Sci.*, 2014, **5**, 2964–2973.

75 P. E. Georghiou and C. K. J. HO, *Can. J. Chem.*, 1989, **67**, 871–876.

76 A. S. Zoolfakar, R. A. Rani, A. J. Morfa, A. P. O'Mullane and K. Kalantar-zadeh, *J. Mater. Chem. C*, 2014, **2**, 5247–5270.

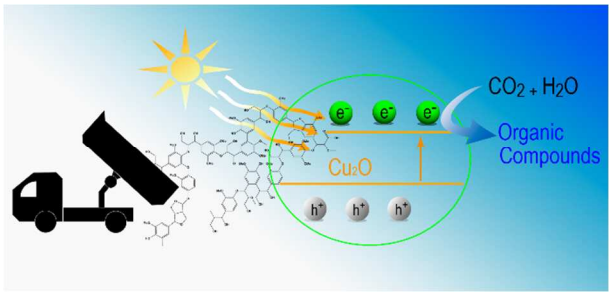

Lignin is a residual product can be reused for stabilize Cu_2O on modified electrodes in CO_2 reduction.